

Macroscale robust superlubricity on metallic NbB₂

Jia Wang

Jilin University

Chang Liu

Jilin University <https://orcid.org/0000-0003-0824-1098>

Kaifei Miao

Jilin University

Kan Zhang (✉ kanzhang@jlu.edu.cn)

Jilin University <https://orcid.org/0000-0003-1354-2784>

Weitao Zheng

State Key Laboratory of Automotive Simulation and Control, Department of Materials Science, Key Laboratory of Automobile Materials of MOE, Jilin University, Changchun

Changfeng Chen

University of Nevada, Las Vegas <https://orcid.org/0000-0002-6110-1118>

Article

Keywords: robust superlubricity, material engineering

Posted Date: May 20th, 2021

DOI: <https://doi.org/10.21203/rs.3.rs-506397/v1>

License:  This work is licensed under a Creative Commons Attribution 4.0 International License.

[Read Full License](#)

Abstract

Robust superlubricity (RSL), defined by concurrent superlow friction and wear, holds great promise for reducing material and energy loss in vast industrial and technological operations. Despite recent advances, challenges remain in finding materials that exhibit RSL on macro length and time scales and possess vigorous electrical conduction ability. Here we report the discovery of RSL on hydrated NbB₂ films that exhibit vanishingly small coefficient of friction (0.001-0.006) and superlow wear rate (~10⁻²² m³/Nm) on large length scales reaching millimeter range and prolonged time scales lasting through extensive loading durations. Moreover, the measured low resistivity (~10⁻⁶ Wm) of the synthesized NbB₂ film indicates ample capability for electrical conduction, extending macroscale RSL to hitherto largely untapped metallic materials. We elucidate pertinent microscopic mechanisms by deciphering the intricate load-driven chemical reactions that generate and sustain the observed superlubricating state and assessing the strong stress responses under diverse strains that produce the superior durability.

Introduction

The material and energy loss due to friction is a serious impediment on industrial and technological production and operation with negative impacts on the environment. Improving the efficiency and durability of moving mechanical parts via lubrication has been an enduring challenge to ancient technologies and modern science and engineering alike. The millennia-old tradition of lubricating contacting surfaces with oil or grease continues to find broad applications in present-day machineries; but developments in materials science have introduced more advanced techniques in treating surfaces via suitable coatings and using a variety of natural and synthetic solid and liquid lubricants. Recent years have seen the emergence and development of a distinct class of materials operating in a remarkable regime of motion known as superlubricity (SL), which is defined by nearly friction-free (friction coefficient less than 0.01) states of motion¹. Major efforts in SL research have focused on materials like graphite²⁻⁴, graphene⁵⁻⁷, hexagonal BN^{8,9} and MoS₂¹⁰⁻¹³ that possess strong intralayer bonding but very weak interlayer interactions, allowing easy sliding motion with small friction, which is further diminished via specially tailored incommensurate interlayer structural alignments. Such so-called structural SL is most viable at nano- to micro-scale where interlayer stacking can be effectively controlled. Extending this approach to larger length scales has faced formidable challenges¹⁴, and elaborate structural designs have been proposed, such as diamond-like carbon (DLC), nanodiamond and graphene¹⁵, and MoS₂ patches¹⁶. Among notable developments in recent years are amorphous carbon films that exhibit SL behaviors under hydrogenation¹⁷ or lubrication with organic friction modifiers¹⁸, while enhanced engineering designs have been proposed based on the combination of amorphous carbon film and additional carbon nanostructures¹⁹.

Another major approach in this research field invokes the concept of liquid based SL state, which can be more easily scaled up to macroscale²⁰. Of particular interest are water-based lubricants^{21,22}, which are more environment friendly than traditional oil-based lubricants. Major examples include acid-²³, ionic

liquid²⁴ and nanomaterial-based aqueous lubricants²⁵⁻²⁷, which operate based on the principles of hydrodynamic lubrication of water, hydrogen-bond network for viscous lubricants, and “stern layer” and hydrogen-bond network for acid-based lubricants²⁰. The use of additives, however, still poses major material and environmental challenges, such as severe wear, acidic conditions and stringent surface preparation requirements. These pressing issues call for cleaner water-based lubrication, which hinges on finding materials that exhibit SL under simple hydration conditions. Additionally, SL materials also need to possess low wear rate for high durability. Many device applications further require the coating materials to conduct electricity, but metallic macroscale SL materials have been conspicuously lacking, leaving this prominent functional demand unattained.

In this article, we report an intriguing discovery of macroscale robust superlubricity (RSL) in metallic transition-metal diboride NbB₂. This outstanding regime of motion is characterized by concurrent superlow friction and wear with exceedingly small friction coefficient of 0.001-0.006 and vanishingly low wear rate around 10⁻²² m³/Nm. Notably, the synthesized NbB₂ film has low measured resistivity on the order of 10⁻⁶ W m, which establishes macroscale RSL for the first time among metallic materials. The observed RSL is generated and sustained by the friction process on the hydrated specimen surface, which is viable in humid ambient environments without requiring chemical additives, thus facilitating practical implementations. We first performed tribological tests on the NbB₂ film using the standard counterpart ball and then used a tailor-made counterpart pin with a greatly enlarged contacting surface area, demonstrating RSL on length scales reaching the state-of-the-art millimeter range for macroscale SL. We elucidate atomistic mechanisms for the observed phenomena by analyzing the key chemical reactions that generate the SL state and assessing the structural and stress responses that maintain the superior structural durability with minimal wear during the friction loading process.

The present findings extend macroscale RSL into the prominent class of metallic materials, enabling applications in diverse equipment and device settings where RSL has not yet been achieved. This work also lays a solid foundation for further exploration and development of additional metallic RSL materials among transition-metal diborides and possibly other related compounds that are capable of operating in maintenance-free and environment friendly conditions, opening paths for new versatile implementations of RSL in a broad variety and range of industrial and technological applications.

Results

Synthesis and characterization of NbB₂ films. We synthesized NbB₂ in thin film on Si substrate using the magnetron sputtering technique and obtained specimens in good crystallinity with the (001) texture in the simple hexagonal structure (Supplementary Fig. S1). We then performed tribotests using a ball-on-disc tribometer as depicted in the inset of Fig. 1a (see Methods for more details). Deionized water droplets were added to the tribopair contact area to hydrate the film surface, resulting in a steady-state water bridge connecting the film surface and the tribometer ball. This solid (tribopairs), liquid (water bridge) and gas (air) three-phase contact mode is highly conducive to generating and sustaining RSL on NbB₂ film

(see below for details). Under the three-phase contact, the friction coefficient of NbB₂ film starts at 0.06-0.07 and declines steadily as the test progresses (Fig. 1a); after a break-in period of 3.5 hours, the friction coefficient drops below 0.01, entering an SL state that lasts for the entire subsequent test period with an average value of 0.0075. The SL state stays robust for the remaining 6.5 hours of the experimental run without any abatement to the end, indicating long-lasting SL induced and maintained by load-driven self-sustaining lubricating mechanisms.

For materials exhibiting SL behaviors, durability is also a prominent consideration for practical applications; a superlow wear rate is therefore another hallmark that is a highly desired and sought-after quality for RSL materials. To assess this characteristic property, we have examined the wear track by taking optical microscope images after the tribotests, and the resulting images show no visible accumulation of wear debris. After a thorough ultrasonic treatment with ethanol, the wear track was observed by a 3D optical profilometer, and the results (Fig. 1b) show only slight and shallow abrasion. An analysis of the cross-sectional depth (Fig. 1c) yields a vanishingly low wear rate of $2.85 \times 10^{-22} \text{ m}^3/\text{Nm}$, which is among the smallest values for durable coating materials. This striking phenomenon is fundamentally rooted in the superior mechanical strength stemming from the strong bonding structure of NbB₂, which underlies both the long break-in period for the onset of SL behaviors and the high durability during frictional loading conditions. We will elucidate the atomistic mechanisms based on systematic first-principles evaluations of the stress-strain relations of NbB₂ later in this article.

To explore the effect of variable degrees of crystallinity on tribological properties, we have prepared NbB₂ films in less crystallized forms and run additional tribotests on such NbB₂ films. The results (Supplementary Fig. S2) show that such films all enter similar SL states with dynamic friction coefficients dropping below 0.01. Interestingly, these less crystallized films require notably reduced amounts of break-in time to enter the SL state, indicating that such structurally weakened NbB₂ films are more conducive to releasing contents that promote the load-driven lubricating mechanism, evincing that the friction products from the NbB₂ films play a major role in generating the SL states.

To assess the electrical conduction capacity of the synthesized NbB₂ film, we have performed four-probe resistance measurements (see Methods for details). The obtained resistivity of $(7.44 \pm 0.24) \times 10^{-7} \text{ } \Omega\text{m}$ indicates good ability for electrical conduction of the NbB₂ film. This result is consistent with the calculated electronic density of states data (see below) that reveal robust metallic nature of NbB₂ both at equilibrium and at large loading strains. It is noted that macroscale SL materials reported to date have been dominated by strong covalent materials, operating in dry or liquid environment²⁰. The first category includes DLC/nanodiamond/graphene¹⁵, DLC/nanodiamond/MoS₂¹⁶, ta-C/ta-C in unsaturated fatty acids or glycerol¹⁸, and fullerene-like MoS₂/steel ball¹⁰; the second category includes Si₃N₄/Si₃N₄ in water²⁸, Si₃N₄/SiC in water²⁹, CN_x/SiC in water³⁰, Si₃N₄/SiO₂ in water containing lubricating additives^{25,27,31}, and Si₃N₄/Si₃N₄ in ionic liquid^{24,32}. These materials are all electrically non-conducting with fairly large electronic band gaps that are typical for strong covalent solids. The presently reported

NbB₂ films with RSL characteristics represent a distinct type of materials that possesses the rare combination of superlow friction and wear rate with good electrical conducting capacity. This finding opens new possibilities for implementing RSL in more versatile applications where vigorous electrical conduction is required.

The RSL of NbB₂ requires no special structural alignment or maintenance at the friction surfaces and, therefore, is expected to scale up readily to large length scales. To verify this idea, we replaced the standard Al₂O₃ counterpart ball, which operates in a point-contact mode, with a tailor-made Al₂O₃ pin that has a circular contacting surface of a 1.00 mm diameter, as shown in Fig. 2a. During the tribotests, the dynamic friction coefficient initially at about 0.02 continues to decline and SL sets in after a 2.8-hour break-in period and lasts for the rest of duration of the test with an average friction coefficient of 0.0082. The optical microscope images shown in Fig. 2b and 2c reveal that the wear track and the pin contact scar show no obvious wear except for some tribo-products. This result shows that the NbB₂ film in the three-phase contact environment can reach the RSL state on the millimeter length scale in a large surface-contact mode.

The present results are expected to open fresh avenues for discovering more RSL materials among metallic compounds, but further advances hinge on a comprehensive understanding of fundamental mechanisms underlying the experimentally observed phenomena. To facilitate this process, we have performed a systematic examination of the tribological procedure and products to analyze the associated atomistic processes. Our analysis reveals key chemical, structural and mechanical properties that underpin the superior tribological characters of the NbB₂ films, which are elaborated below.

Mechanism for superlubricity of hydrated NbB₂. To elucidate atomistic mechanisms for the SL state of hydrated NbB₂, we have performed a thorough analysis of the friction surfaces following the tribotests. We have carried out Raman characterization on two distinct areas, one away and another at the center of the wear track. In the first case, weak H₃BO₃ (620 cm⁻¹)³³ and Nb₂O₅ (235, 314 and 470 cm⁻¹)^{34,35} peaks are detected, as shown in Fig. 3b, indicating oxidation of the film surface that is exposed to ambient air. In contrast, a notably stronger Nb₂O₅ peak (250 cm⁻¹)³⁶ accompanied by two weak Nb₂O₅ peaks (470 and 880 cm⁻¹)^{34,35} appear in the spectra taken at the wear track center, indicating that a large amount of Nb₂O₅ has formed during the tribotests. Additionally, two very strong H₃BO₃ peaks (610 and 975 cm⁻¹)^{33,37} are detected, indicating that H₃BO₃ is among the main oxidative products generated by the friction process.

To corroborate the above bonding assignments based on the Raman spectra, we have further performed x-ray photoelectron spectroscopy (XPS) measurements of the wear track. The results (Fig. 3c) show that in addition to the spectral features attributed to the bonds in the original NbB₂ film, the B 1s and Nb 3d spectra reveal B-O bonds in H₃BO₃ and Nb-O 3d_{5/2} and Nb-O 3d_{3/2} bonds in Nb₂O₅. Moreover, we examined the tribo-products collected from the wear scar center of the counterpart ball and observed the Raman peaks of H₃BO₃ (617, 1105, 1365 and 1449 cm⁻¹)^{37,38} and Nb₂O₅ (235, 306, 390, 485 and 845 cm⁻¹)^{34,35}.

¹⁾^{34,35} (Fig. 3b). These results offer compelling evidence on substantial friction generated H₃BO₃ and Nb₂O₅, which help promote the SL state at the surface of the NbB₂ film. Meanwhile, tribotests in dry or water-covered environments also produce H₃BO₃ and Nb₂O₅ yet fail to produce SL states (Supplementary Fig. S3), indicating that additional conditions need to be met to induce superlubricity.

Friction induced tribo-products dissolve into the “water bridge” to produce a certain concentration of charged colloids via the Tyndall effect (Supplementary Fig. S4). The average zeta potential of the “water bridge” content collected after the tribotests is about -8.45 mV, clearly indicating that it is negatively charged (Supplementary Fig. S5). The Fourier-transform infrared (FTIR) spectrum of this tribo-liquid (Fig. 3d) reveals that besides the peak associated with the O-H bond (3368.17 cm⁻¹), there exist distinct peaks of H₃BO₃ (545.19, 654.31 and 809.19 cm⁻¹) and Nb₂O₅ (1644.29 cm⁻¹)^{33,39,40}. High-resolution transmission electron microscopy (HRTEM) measurements (Fig. 3e) show small particles well dispersed in an amorphous matrix without aggregation. These dispersed particles comprise crystalline Nb₂O₅ grains, which are well matched with the (101) oriented orthorhombic-Nb₂O₅ crystallites. Averaging results from more than 100 particles, the size distribution is *ca.*2.5 nm on average and 2.25~3 nm in range with the measurement result of 2.25 nm accounting for nearly 50% of the particles. It is noted that the identified amorphous matrix is not completely disordered but rather displays small curved layers with fingerprint-like structures. Furthermore, the interlamellar spacing of the short-range ordered layer with fingerprint-like structures is about 3.19 Å, which is well matched with the structural feature of H₃BO₃, so the characteristic fingerprint-like structures likely stem from the formation of H₃BO₃ lamellae after the evaporation of water. These results identify H₃BO₃ and Nb₂O₅ colloidal particles as key agents that work synergistically at the friction surfaces to achieve superlubricity.

We now present an in-depth analysis of the three-phase contact environment at the surface of NbB₂. As depicted in Fig. 4(a-c), promoted by friction, the wear surface of NbB₂ undergoes an oxidation reaction with O₂ in the air, generating B₂O₃ and Nb₂O₅, and the intermediate oxidative product (B₂O₃) further reacts with H₂O to form H₃BO₃. The total reaction process is described by $4\text{NbB}_2 + 12\text{H}_2\text{O} + 11\text{O}_2 \rightarrow 8\text{H}_3\text{BO}_3 + 2\text{Nb}_2\text{O}_5$ (Equation 1). The resulting tribo-products dissolve in the “water bridge”, producing a tribo-liquid containing a large amount of H₃BO₃ and Nb₂O₅ in the 4:1 ratio. As a typical monobasic weak acid, the H₃BO₃ easily ionizes in water, generating tetrahydroxy borate ions in the B-centered tetra-coordinate units (B(OH)₄⁻) and hydrogen ion (H⁺) via the reaction $\text{B}(\text{HO})_3 + \text{H}_2\text{O} \rightarrow \text{B}(\text{OH})_4^- + \text{H}^+$ (Equation 2). The ionization of H₃BO₃ acts as an ongoing source of H⁺, which is absorbed by Nb₂O₅ to form positively charged colloidal particles (Nb₂O₅)·*n*H⁺ via reaction $\text{Nb}_2\text{O}_5 + n\text{H}^+ \rightarrow (\text{Nb}_2\text{O}_5) \cdot n\text{H}^+$ (Equation 3), further promoting the forward ionization reaction. The resulting tribo-liquid contains ample B(OH)₄⁻, (Nb₂O₅)·*n*H⁺ and H₃BO₃ generated by these tribochemical reactions.

Our post-tribotest characterization has uncovered strong evidence of ample Nb₂O₅ and H₃BO₃ on the NbB₂ surface. During friction, the three reactions described above reach a dynamic equilibrium. From

Equations 1 and 2 and the conservation of reaction, the content of $B(OH)_4^-$ is much higher than that of $(Nb_2O_5) \cdot nH^+$. At the friction surface positively charged $(Nb_2O_5) \cdot nH^+$ ions interact with negatively charged $B(OH)_4^-$ ions to form $(Nb_2O_5) \cdot nH^+ \cdot mB(OH)_4^-$ via $(Nb_2O_5) \cdot nH^+ + mB(OH)_4^- \rightarrow (Nb_2O_5) \cdot nH^+ \cdot mB(OH)_4^-$ (Equation 4, see the depiction in Fig. 4d). Size effects of $B(OH)_4^-$ prevent proportional reaction, so m is less than n in the above equation. Therefore, stable tribo-liquids at the friction surface contain $(Nb_2O_5) \cdot nH^+ \cdot mB(OH)_4^-$ and a large number of free $B(OH)_4^-$ (Fig. 4e). These ingredients bond with water molecules through the hydrogen bonding, and the $B(OH)_4^-$ ions help neutralize $(Nb_2O_5) \cdot nH^+$ ions at the friction surface. Moreover, the tribo-products on tribopair surfaces can fix a portion of water molecules to form a hydration layer⁴¹ that coexists with a flowing hydration layer containing tribo-products between the upper and lower fixed hydration layers, as shown in Fig. 4f. Overall, the number of negatively charged surface sites is greater than that of positively charged sites, making both friction surfaces net negatively charged. Meanwhile, the flowing hydration layer contains ample $B(OH)_4^-$ ions, leading to an electrical double-layer repulsion between the flowing hydration layer and the two fixed hydration layers, reducing the contact pressure. Consequently, the flowing hydration layer exhibits its natural weak shear characteristics to produce the observed small friction^{21,42}. Overall, two factors are key to generating SL at the NbB_2 surface: (i) tribo-products displaying hydrophilic properties to enable the formation of fixed hydration layers on the friction surface and (ii) charged agents from tribochemical reactions generating interface and hydration layer repulsion to unleash the weak shear character of the tribo-liquid.

Mechanism for the superlow wear rate of NbB_2 . Transition-metal borides possess very high mechanical strength stemming from their superior bonding structure, with the transition-metal atoms provide a high count of valence electrons to resist compression and boron atoms form a strong covalent network to sustain large shear deformation⁴³. To elucidate the atomistic mechanisms for the superlow wear rate of NbB_2 , we have performed quantum mechanical calculations to examine the stress responses of NbB_2 under the friction induced biaxial stress that comprises a shear stress component aligned in the frictional contact surface and a compressive stress normal to the contact surface. We have performed systematic calculations of stress-strain relations to assess pertinent mechanical properties [see Methods for computational details]. This approach has been broadly employed in the study of many transition-metal compounds, including a wide range of borides, and the results have provided accurate descriptions of a variety of structural and mechanical properties⁴⁴⁻⁴⁸ and proved to be a powerful tool in probing and elucidating prominent structure-property relations of wide-ranging materials under versatile loading conditions⁴⁹⁻⁵².

To assess the atomistic mechanisms underlying the superlow wear rate of NbB_2 observed in our tribotests, we have examined stress responses to frictional shear strains applied to the (001) oriented NbB_2 specimen, which is the structural configuration of the synthesized and tested specimen (see Fig. 5a for the bonding structure in the (001) oriented NbB_2). Our calculations first establish the stress responses under the pure shear strains along the high-symmetry (001)[100] and (001)[210] slip directions to set the

key benchmarks on the strength and toughness. The calculated results (see Figs. 5c and 5d) reveal strong stress responses to the pure shear deformations, with the peak shear stresses reaching 37-38 GPa in the two major slip directions. The bonding structure in the NbB₂ (001) plane has a six-fold rotational symmetry, which produces a densely packed and evenly spanned 12-fold shear-slip directions, as indicated by the two sets of colored arrows in Fig. 5a, that make the (001) oriented NbB₂ specimen strongly resistant to shear deformations. Moreover, after the initial steep rise, the stresses remain high and form extended plateaus over large strain ranges in both shear slip directions, which further enhances the strong and tough nature of the NbB₂ crystal under these loading conditions. These remarkable mechanical characteristics can be attributed to the mixed metallic and covalent nature of the bonds in NbB₂ that play prominent roles in determining the strength and toughness of the crystal. To elucidate the pertinent underlying atomistic mechanism, we have analyzed the bonding changes in response to the applied shear strains. We present in Fig. 5b the bonding configuration of NbB₂ at the peak stress under the (001)[100] pure shear strains compared with the bonding structure at equilibrium, and the results show that the mixed covalent-metallic Nb-B bonds tilted in the shear-slip direction undergo the most elongation and act as the major load-bearing bonds under the shear loading. Similar changes occur consistently in bonding configurations with the Nb-B bonds tilted in the shear-slip direction as the major load bearers under all the pure shear and biaxial strains examined in this work. These results explain the simultaneously strong and tough stress responses under diverse loading conditions in all the cases shown in Figs. 5c and 5d.

Under the frictional loading conditions during the tribotests, the (001) oriented NbB₂ crystal is subjected to the coexisting shear and normal stresses in a flat-contact geometry. Accordingly, we have further calculated the shear stress responses in the presence of a flat-contact normal stress that is omnipresent in such contact modes to assess the structural deformation modes and the associated mechanical strength that determine the durability of the synthesized NbB₂ specimen. The obtained results (see Fig. 5c and 5d) reveal consistently enhanced shear stresses at rising normal stresses, showcasing notable strain stiffening of NbB₂ under the frictional contact environments. This load induced strengthening phenomenon is extraordinary among TM compounds, many of which are known to suffer the opposite effect, namely strain softening⁴⁴⁻⁴⁷. Moreover, the extended plateaus seen in the pure-shear stress curves, indicating high toughness, remain robust under the normal-stress constrained shear strains of frictional loadings. This behavior underscores the concurrent superior mechanical strength and toughness of NbB₂ under the tribotest loadings, offering key insights into the atomistic mechanism for the exceptional durability as manifested in its superlow wear rate.

Electronic density of states of metallic NbB₂ under diverse strains. To evaluate the capability for electrical conduction of the synthesized specimen under the various pure shear and biaxial frictional strains in comparison with the result of the unstrained crystal, we have calculated the electronic density of states of NbB₂ under the related loading conditions. We present in Fig. 5e the electronic density of states near the Fermi level under several representative loading conditions, including NbB₂ crystal at unstrained

equilibrium structure, deformed at the peak pure-shear stresses along the (001)[100] and (001)[210] shear slip directions, and under the biaxial strains with the normal stress $s_{zz} = 5$ GPa along the two selected shear slip directions. These results show that the electronic states around the Fermi level of the deformed crystal remain rigorous and increase slightly, indicating that the good electrical conduction ability of the synthesized NbB₂ specimen in the unstrained equilibrium configuration determined by the four-probe resistance measurements presented above will remain robust under versatile loading conditions and persist to large strains encompassing the full elastic ranges. This result bodes well for meeting the requirement of consistently good electrical conduction in many device applications under diverse operational environments.

Discussion

The present work demonstrates macroscale robust superlubricity of metallic NbB₂, which may be extended to other transition-metal diborides that share the same material characters for achieving similar tribological performance with the exceptionally low friction and wear characters. Further exploration of these compounds is expected to produce better understanding of the effects of different chemical composition involving different transition-metal atoms on the efficacy of the resulting tribo-liquid for reducing friction at the three-phase contact; another aspect of interest is a systematic examination of the effects of different transition metals on the structural and mechanical responses to friction loadings, which hold key to producing the superlow wear rate. We are hopeful that the present findings will stimulate further investigations of these key issues that may help find additional transition-metal diborides that exhibit RSL behaviors.

The RSL of NbB₂ is obtained under hydrated conditions characterized by a “water bridge” configuration formed at the dynamic friction surfaces in ambient environment. The combination of solid NbB₂, tribo-liquid, and ambient air comprises a three-phase contact state that promotes tribochemical reactions producing H₃BO₃ and Nb₂O₅, which are continuously generated and dispersed into the “water bridge” for the formation of ionic $(\text{Nb}_2\text{O}_5) \cdot n\text{H}^+ \cdot m\text{B}(\text{OH})_4^-$ and $\text{B}(\text{OH})_4^-$, which are the crucial components of the tribo-liquid generating and sustaining RSL. This load-generated and self-sustaining mechanism is highly robust and conducive to RSL on large length and time scales, as demonstrated in our experiments, making NbB₂ and possibly additional transition-metal diborides suitable for practical implementation in diverse applications.

Achieving the RSL state on NbB₂ requires adequate surface hydration, because the tribochemical reactions for oxidation, ionization, adsorption and complexation depend on properly supplied water. Otherwise, those reactions will proceed in reverse, and the tribological behaviors will display the characteristics of dry friction. In tribotests presented above, water droplets were added to the contacting interface between the tribopairs to facilitate the process. To verify the feasibility of truly self-sustainable RSL, we have set up a controlled environment where a humidifier was used to generate humid air in a CSM tribotest chamber enclosed by a cover to retain the moisture, replacing dripping water as the source

for hydrating the surface of NbB₂ specimen. When the humidity inside the chamber rises above 93%, gathering moisture at the interface of tribopairs quickly condense and form a “water bridge” (Supplementary Fig. S6). This finding indicates that high environmental humidity may be a viable source for the three-phase contact formation at the sliding contact. Such a “water bridge” also should be able to form in lower humidity environments over longer time period to allow sufficient water condensation at the tribopair interface. These observations and inferences bode well for implementing RSL in diverse controlled or natural humid environments.

This work establishes NbB₂ as a distinct RSL material with concurrent possession of superlow friction, superlow wear and good electrical conducting capacity, thereby offering a highly desirable combination of performance characteristics that are needed in wide-ranging device and equipment settings. An in-depth analysis unveils the friction-driven chemical reactions at the hydrated NbB₂ surface in ambient air and the superior strengths under the frictional loading conditions stemming from the intrinsic strong bonding characters of NbB₂ crystal as key microscopic mechanisms for the observed phenomena. These fundamental physics and chemistry insights may guide rational exploration and discovery of additional transition-metal diborides and related compounds that exhibit metallic RSL behaviors on the macroscale. We expect that the present study will stimulate considerable interest and efforts for further research leading to vigorous development and implementation of RSL in versatile applications.

Methods

Synthesis of the NbB₂ film. We deposited NbB₂ films on mirror-polished n-type Si (100) wafers by magnetron sputtering NbB₂ target in a high-vacuum system with a base pressure of 5×10^{-4} Pa. The Si substrates were ultrasonically cleaned in subsequent baths of acetone, ethanol and deionized water for 20 min, then blown dry with N₂ before deposition. During deposition, the working pressure was maintained around 0.7 Pa via controlling the flow rate of Ar at 80 sccm; the sputtering power on the NbB₂ target was kept constant at 90 W (sputtering current at ~ 0.3 A) by a DC power supply. Additionally, a -80 V bias voltage and a temperature of 400 °C were applied on the substrates during deposition. The target-substrate distance and substrate rotational speed were fixed at 80 mm and 10 r/min, respectively. An interlayer (Nb/NbN) was first deposited to enhance the film-substrate adhesion.

Structure and morphology characterization. By using a D8-tools Bragg-Brentano diffractometer with a Cu-K α line ($\lambda = 1.54056$ Å), X-ray diffraction (XRD) in the θ - 2θ mode was conducted and the structural properties (such as interplanar spacing, crystal orientation, and grain size) of NbB₂ were measured. The microstructure was obtained by high-resolution transmission electron microscopy (HRTEM) using a field-emission JEOL 2010F microscope operated at 200 kV; the sheet specimen for the HRTEM measurement was prepared by mechanically scratching the NbB₂ surface with a clean stainless-steel blade. Analyses of composition and chemical states were carried out via PerkinElmer PHI-5702 X-ray photoelectron spectroscopy (XPS); before measurement, 15 min Ar⁺ etching (1 keV etching energy) was carried out to remove any surface contaminants. Subsequently, the sectional measurements of NbB₂ were conducted

via SU 8010 scanning electron microscope (SEM) to explore the film growth condition. The corresponding surface morphology and root-mean-square roughness (R_q) were obtained from using an atomic force microscope (AFM, Dimension Icon, Veeco Instruments, Bruker, Germany). The thickness of film was measured by Veeco Dektak 150 surface profiler. In addition, to determine the hardness and elasticity modulus of NbB_2 , we performed nanoindentation measurement with a penetration depth of 500 nm by MTS Nanoindenter XP with a 3-side pyramidal Berkovich-type diamond indenter.

Tribotests and post-friction characterizations. Tribotests of NbB_2 were performed using a CSM ball-on-disk macroscale tribometer along a circular track of 5 mm diameter against the Al_2O_3 ball (diameter of 6 mm and Rockwell Hardness of 80). During the tribotests the normal load was kept at 1 N and the sliding speed at 1.0 cm/s. Prior to the start of the tests, a pipette was used to drip about 5 μL of deionized water on the film surface to construct the three-phase contact environment between the friction surfaces. Besides, friction tests in normal dry atmospheric environment and in a full water-covered environment at room temperature were also performed to assess their influence on the tribological behaviors of NbB_2 . After the tribotests, ex situ characterization and analysis of the worn surface were performed using a 3D optical profilometer (Bruker ContourGT). The wear rate was calculated from the volume of the removed material by measuring the cross-sectional area at five different locations along the wear track. Further identifications were carried out to recognize the chemical composition of the wear track and wear scar by Raman spectroscopy (Renishaw 1000, 514.5 nm laser) with an output power of 2 W, and to analyze the relative content of the oxidation products by XPS carried out at the wear track after the tribotests. Also, the information about the surface of the wear track and wear scar was acquired by optical digital microscope (OLLYMPUS DSX510). The “tribo-liquid” formed during the friction process was collected by a pipette for characterization via irradiation by infrared light to detect the Tyndall effect. The FT-IR spectrum of “tribo-liquid” was obtained on an ALPHA Fourier Transform Infrared Spectrometer (Bruker) with the ATR mode. Dropping the “tribo-liquid” on Cu grids and letting water evaporate completely, the microstructures of colloidal particles in the “tribo-liquid” were observed by HRTEM. The Zeta potential measurement of the “tribo-liquid” was performed by using a nanoparticle potentiometer (Zetasizer Nano ZS).

First-principles calculations for stress-strain relations. First-principles calculations were performed using the VASP code⁵³ and adopting the projector augmented wave method⁵⁴ and local density approximation with the exchange-correlation functional of Ceperley and Alder⁵⁵ as parametrized by Perdew and Zunger⁵⁶. An energy cutoff of 800 eV and a Monkhorst-Pack grid⁵⁷ with a maximum spacing of 0.18 \AA^{-1} are adopted, achieving an energy convergence around 1 meV per atom.

The stress-strain relations under biaxial stress states that contains a shear stress and a normal compressive stress component. This approach recovers the pure shear case in the limit of zero normal stress and generally simulates indentation processes^{49,58,59}. The shape of the (deformed) unit cell and atomic relaxation are determined completely at each step by the constrained structural optimization. The starting position for each strain step is taken from the relaxed coordinates of the previous strain step to

ensure the quasistatic strain path, with a strain increment of 0.01. At each step, the applied shear strain is fixed to determine the shear stress s_{xz} , while the other five independent components of the strain tensors and all the atoms inside the unit cell are simultaneously relaxed until the compressive stress component reaches $s_{zz}=c$, where c is a constant normal compressive stress; meanwhile, all other four components of the Hellmann-Feynman stress tensor and the force on each atom become less than 0.1 GPa and 0.005 eV/Å⁻¹, respectively.

Declarations

Acknowledgements

This work was supported by the National Natural Science Foundation of China (Grant Nos. 51972139, 51602122, 51905206), National Key R&D Program of China (Grant No. 2016YFA0200400), the China Postdoctoral Science Foundation (Grant No. 2020M681031), the Program for JLU Science and Technology Innovative Research Team (2017TD-09), the Fundamental Research Funds for the Central Universities, and the High-Performance Computing Center of Jilin University, China.

Author contributions

K.Z. conceived the project; K.Z. and J.W. directed the experimental efforts; K.M. performed sample preparation, measurements and data processing, and J.W. and K.Z. assisted with the measurements and data analysis; C.L. directed the modeling and computational efforts and performed the calculations and associated data analysis; all authors contributed to the discussion of the results; J.W., C.L., K.Z. and C.C. wrote the paper with input from all authors.

Corresponding author

Kan Zhang (kanzhang@jlu.edu.cn)

Competing interests

The authors declare no competing interests.

Data availability

The data that support the findings of this study are available from the corresponding authors upon reasonable request.

Supplementary information

Experimental details and additional supporting results.

References

- 1 Hod, O., Meyer, E., Zheng, Q. & Urbakh, M. Structural superlubricity and ultralow friction across the length scales. *Nature* **563**, 485-492 (2018).
- 2 Dienwiebel, M. *et al.* Superlubricity of graphite. *Phys. Rev. Lett.* **92**, 126101 (2004).
- 3 Li, J., Li, J. & Luo, J. Superlubricity of Graphite Sliding against Graphene Nanoflake under Ultrahigh Contact Pressure. *Adv. Sci. (Weinh)* **5**, 1800810 (2018).
- 4 Deng, H., Ma, M., Song, Y., He, Q. & Zheng, Q. Structural superlubricity in graphite flakes assembled under ambient conditions. *Nanoscale* **10**, 14314-14320 (2018).
- 5 Feng, X., Kwon, S., Park, J. Y. & Salmeron, M. Superlubric sliding of graphene nanoflakes on graphene. *Acs Nano* **7**, 1718-1724 (2013).
- 6 Kawai, S. *et al.* Superlubricity of graphene nanoribbons on gold surfaces. *Science* **351**, 957-961 (2016).
- 7 Androulidakis, C., Koukaras, E. N., Paterakis, G., Trakakis, G. & Galiotis, C. Tunable macroscale structural superlubricity in two-layer graphene via strain engineering. *Nat. Commun.* **11**, 1595 (2020).
- 8 Song, Y. *et al.* Robust microscale superlubricity in graphite/hexagonal boron nitride layered heterojunctions. *Nat. Mater.* **17**, 894-899 (2018).
- 9 Mandelli, D., Ouyang, W., Hod, O. & Urbakh, M. Negative Friction Coefficients in Superlubric Graphite–Hexagonal Boron Nitride Heterojunctions. *Phys. Rev. Lett.* **122** (2019).
- 10 Chhowalla, M. & Amaratunga, G. A. J. Thin films of fullerene-like MoS₂ nanoparticles with ultra-low friction and wear. *Nature* **407**, 164-167 (2000).
- 11 Wang, L. F. *et al.* Superlubricity of two-dimensional fluorographene/MoS₂ heterostructure: a first-principles study. *Nanotechnology* **25**, 385701 (2014).
- 12 Wang, L. *et al.* Superlubricity of a graphene/MoS₂ heterostructure: a combined experimental and DFT study. *Nanoscale* **9**, 10846-10853 (2017).
- 13 Li, H. *et al.* Superlubricity between MoS₂ Monolayers. *Adv. Mater.* **29**, 1701474 (2017).
- 14 Berman, D., Erdemir, A. & Sumant, A. V. Approaches for Achieving Superlubricity in Two-Dimensional Materials. *Acs Nano* **12**, 2122-2137 (2018).
- 15 Berman, D., Deshmukh, S. A., Sankaranarayanan, S. K., Erdemir, A. & Sumant, A. V. Macroscale superlubricity enabled by graphene nanoscroll formation. *Science* **348**, 1118-1122 (2015).
- 16 Berman, D. *et al.* Operando tribochemical formation of onion-like-carbon leads to macroscale superlubricity. *Nat. Commun.* **9**, 1164 (2018).

- 17 Chen, X. *et al.* Evolution of tribo-induced interfacial nanostructures governing superlubricity in a-C:H and a-C:H:Si films. *Nat. Commun.* **8**, 1675 (2017).
- 18 Kuwahara, T. *et al.* Mechano-chemical decomposition of organic friction modifiers with multiple reactive centres induces superlubricity of ta-C. *Nat. Commun.* **10**, 151 (2019).
- 19 Wang, Y., Gao, K., Zhang, B., Wang, Q. & Zhang, J. Structure effects of sp²-rich carbon films under super-low friction contact. *Carbon* **137**, 49-56 (2018).
- 20 Ge, X., Li, J. & Luo, J. Macroscale Superlubricity Achieved With Various Liquid Molecules: A Review. *Front. Mech. Eng-PRC* **5** 1-15 (2019).
- 21 Ma, L., Gaisinskaya-Kipnis, A., Kampf, N. & Klein, J. Origins of hydration lubrication. *Nat. Commun.* **6**, 6060 (2015).
- 22 Seror, J., Zhu, L., Goldberg, R., Day, A. J. & Klein, J. Supramolecular synergy in the boundary lubrication of synovial joints. *Nat. Commun.* **6**, 6497 (2015).
- 23 Li, J., Zhang, C., Ma, L., Liu, Y. & Luo, J. Superlubricity achieved with mixtures of acids and glycerol. *Langmuir* **29**, 271-275 (2013).
- 24 Ge, X., Li, J., Zhang, C., Liu, Y. & Luo, J. Superlubricity and Antiwear Properties of In Situ-Formed Ionic Liquids at Ceramic Interfaces Induced by Tribochemical Reactions. *ACS Appl. Mater. Inter.* **11**, 6568-6574 (2019).
- 25 Wang, W., Xie, G. & Luo, J. Superlubricity of Black Phosphorus as Lubricant Additive. *ACS Appl. Mater. Inter.* **10**, 43203-43210 (2018).
- 26 Li, J., Cao, W., Li, J., Ma, M. & Luo, J. Molecular Origin of Superlubricity between Graphene and a Highly Hydrophobic Surface in Water. *J. Phys. Chem. Lett.* **10**, 2978-2984 (2019).
- 27 Wang, H. *et al.* Superlubricity of Polyalkylene Glycol Aqueous Solutions Enabled by Ultrathin Layered Double Hydroxide Nanosheets. *ACS Appl. Mater. Inter.* **11**, 20249-20256 (2019).
- 28 Xu, J. & Kato, K. Formation of tribochemical layer of ceramics sliding in water and its role for low friction. *Wear* **245**, 61-75 (2000).
- 29 Chen, M., Kato, K. & Adachi, K. Friction and wear of self-mated SiC and Si₃N₄ sliding in water. *Wear* **250**, 246-255 (2001).
- 30 Zhou, F., Kato, K. & Adachi, K. Friction and wear properties of CN_x/SiC in water lubrication. *Tribol. Lett.* **18**, 153-163 (2005).
- 31 Ge, X., Li, J., Luo, R., Zhang, C. & Luo, J. Macroscale Superlubricity Enabled by the Synergy Effect of Graphene-Oxide Nanoflakes and Ethanediol. *ACS Appl. Mater. Inter.* **10**, 40863-40870 (2018).

- 32 Ge, X. *et al.* Macroscale superlubricity under extreme pressure enabled by the combination of graphene-oxide nanosheets with ionic liquid. *Carbon* **151**, 76-83 (2019).
- 33 Jun, L., Shuping, X. & Shiyang, G. FT-IR and Raman spectroscopic study of hydrated borates. *Spectrochim. Acta A* **51**, 519-532 (1995).
- 34 Soares, M. R. N. *et al.* Effect of processing method on physical properties of Nb₂O₅. *J. Eur. Ceram. Soc.* **31**, 501-506 (2011).
- 35 Li, S. *et al.* Controllable synthesis of uniform mesoporous H-Nb₂O₅/rGO nanocomposites for advanced lithium ion hybrid supercapacitors. *J. Mater. Chem. A* **7**, 693-703 (2019).
- 36 Pittman, R. M. & Bell, A. T. Raman studies of the structure of niobium oxide/titanium oxide (Nb₂O₅. TiO₂). *J. Phys. Chem.* **97**, 12178-12185 (1993).
- 37 Thomas, R. Determination of the H₃BO₃ concentration in fluid and melt inclusions in granite pegmatites by laser Raman microprobe spectroscopy. *Am. Mineral.* **87**, 56-68 (2002).
- 38 Servoss, R. R. & Clark, H. M. Vibrational Spectra of Normal and Isotopically Labeled Boric Acid. *J. Chem. Phys.* **26**, 1175-1178 (1957).
- 39 Libowitzky, E. & Rossman, G. R. An IR absorption calibration for water in minerals. *Am. Mineral.* **82**, 1111-1115 (1997).
- 40 Prado, A. G. S., Bolzon, L. B., Pedroso, C. P., Moura, A. O. & Costa, L. L. Nb₂O₅ as efficient and recyclable photocatalyst for indigo carmine degradation. *Appl. Catal. B-Environ.* **82**, 219-224 (2008).
- 41 Li, J., Zhang, C., Sun, L., Lu, X. & Luo, J. Tribochemistry and superlubricity induced by hydrogen ions. *Langmuir* **28**, 15816-15823 (2012).
- 42 Han, T. *et al.* Origins of Superlubricity Promoted by Hydrated Multivalent Ions. *J. Phys. Chem. Lett.* **11**, 184-190 (2020).
- 43 Kaner, R. B., Gilman, J. J. & Tolbert, S. H. Designing superhard materials. *Science* **308**, 1268-1269 (2005).
- 44 Zang, C., Sun, H. & Chen, C. Unexpectedly low indentation strength of WB₃ and MoB₃ from first principles. *Phys. Rev. B* **86**, 180101 (2012).
- 45 Zang, C., Sun, H., Tse, J. S. & Chen, C. Indentation strength of ultraincompressible rhenium boride, carbide, and nitride from first-principles calculations. *Phys. Rev. B* **86**, 014108 (2012).
- 46 Li, B., Sun, H., Zang, C. & Chen, C. Fundamental constraints on the strength of transition-metal borides: The case of CrB₄. *Phys. Rev. B* **87**, 174106 (2013).

- 47 Li, B., Sun, H. & Chen, C. First-principles calculation of the indentation strength of FeB₄. *Phys. Rev. B* **90**, 014106 (2014).
- 48 Gong, W. *et al.* Unravelling the structure and strength of the highest boride of tungsten WB₄.2. *Phy. Rev. B* **100**, 220102 (2019).
- 49 Li, B., Sun, H. & Chen, C. Large indentation strain-stiffening in nanotwinned cubic boron nitride. *Nat. Commun.* **5**, 4965 (2014).
- 50 Li, B., Sun, H. & Chen, C. Extreme Mechanics of Probing the Ultimate Strength of Nanotwinned Diamond. *Phys. Rev. Lett.* **117**, 116103 (2016).
- 51 Liu, C., Song, X., Li, Q., Ma, Y. & Chen, C. Smooth Flow in Diamond: Atomistic Ductility and Electronic Conductivity. *Phys. Rev. Lett.* **123**, 195504 (2019).
- 52 Liu, C., Song, X., Li, Q., Ma, Y. & Chen, C. Superconductivity in Compression-Shear Deformed Diamond. *Phys. Rev. Lett.* **124**, 147001 (2020).
- 53 Kresse, G. G. & Furthmüller, J. J. Efficient Iterative Schemes for Ab Initio Total-Energy Calculations Using a Plane-Wave Basis Set. *Phys. Rev. B* **54**, 11169 (1996).
- 54 Kresse, G. & Joubert, D. From ultrasoft pseudopotentials to the projector augmented-wave method. *Phys. Rev. B* **59**, 1758-1775 (1999).
- 55 Ce Perley, D. M. & Alder, B. J. Ground State of the Electron Gas by a Stochastic Method. *Phys. Rev. Lett.* **45**, 566–569 (1980).
- 56 Perdew, J. P. & Zunger, A. Self-Interaction Correction to Density-Functional Approximations for Many-Body Systems. *Phys. Rev. B* **23**, 5048-5079 (1981).
- 57 Monkhorst, H. J. & Pack, J. D. Special points for Brillouin-zone integrations. *Phys. Rev. B* **13**, 5188-5192 (1976).
- 58 Pan, Z., Sun, H. & Chen, C. Colossal shear-strength enhancement of low-density cubic BC₂N by nanoindentation. *Phys. Rev. Lett.* **98**, 135505 (2007).
- 59 Pan, Z., Sun, H., Zhang, Y. & Chen, C. Harder than diamond: superior indentation strength of wurtzite BN and lonsdaleite. *Phys. Rev. Lett.* **102**, 055503 (2009).

Figures

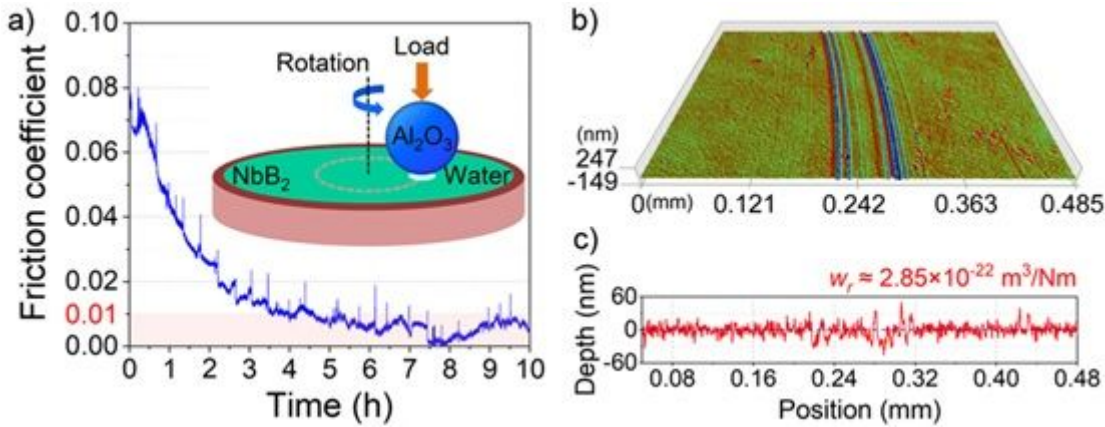


Figure 1

Tribological characterization of the NbB_2 film in the ball-on-disk mode. (a) Dynamic friction coefficient of the highly crystallized NbB_2 film measured in the ball-on-disk mode. The inset is a schematic diagram of the ball-on-disk tribotest setup in the film-water-air three-phase contact mode. After a break-in period of about 3.5 hours, the friction coefficient drops below 0.01, entering an SL state that lasts for the subsequent 6.5-hour test duration with an average friction coefficient of 0.0075. No abatement of the SL state is seen to the end of the tribotest, indicating a long-lasting load-driven and sustained SL mechanism. (b) A 3D profile image and (c) a cross-sectional view of the NbB_2 film wear track taken after the 10-hour tribotest. To measure the abrasion state, the film is ultrasound treated with ethanol before taking the 3D profile and cross-sectional characterizations. The wear rate of $2.85 \times 10^{-22} \text{ m}^3/\text{Nm}$ for the NbB_2 film is calculated by fitting the cross-sectional data.

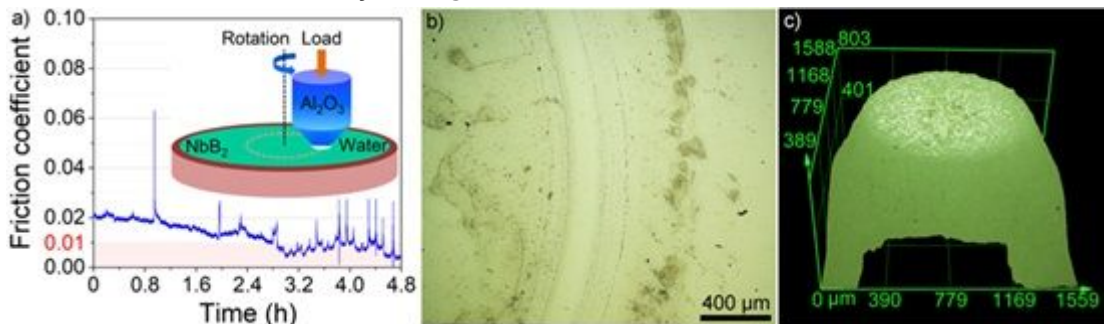


Figure 2

Tribological characterization of the NbB_2 film in the pin-on-disk mode. (a) Dynamic friction coefficient of the highly crystallized NbB_2 film measured in the pin-on-disk mode. The inset is a schematic diagram of the pin-on-disk tribotest setup in the three-phase contact mode. The Al_2O_3 counterpart pin has a diameter of 1 mm. Superlubricity occurs after a 2.8-h break-in period and remains unabated for the rest of the tribotest period with an average friction coefficient of 0.0082. Also shown are the optical microscope images of (b) the NbB_2 film wear track and (c) the counterpart pin wear scar taken without any pre-processing.

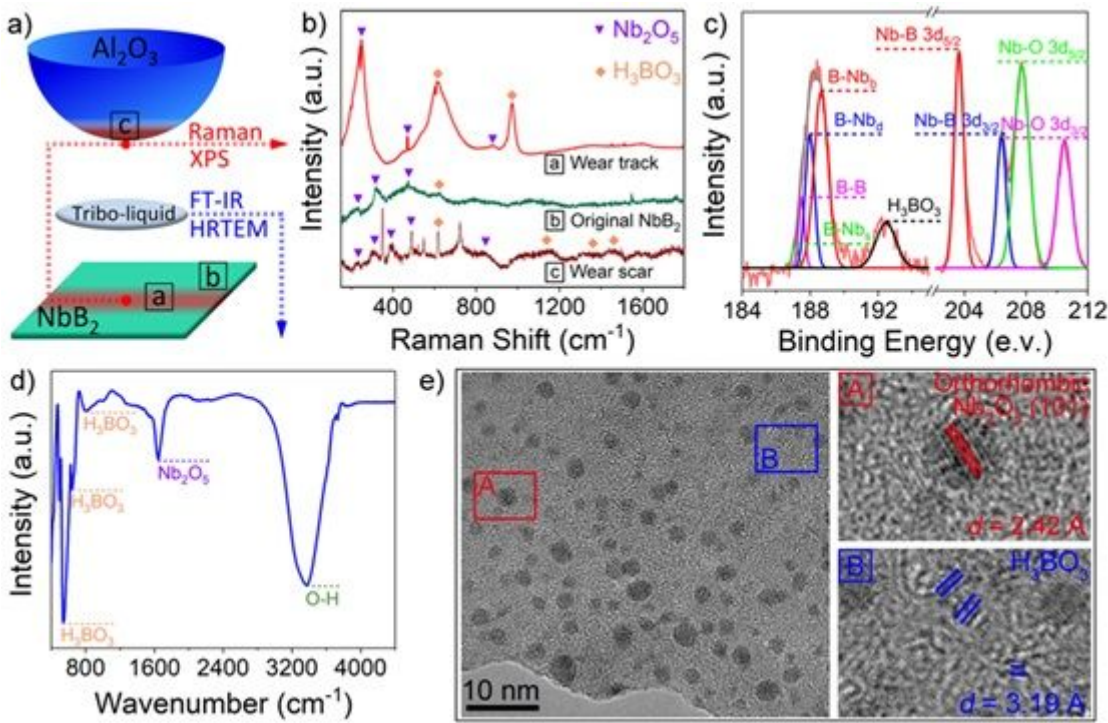


Figure 3

Post-tribotest characterization of the NbB₂ film wear track, counterpart ball wear scar and tribo-liquid. (a) Schematic diagram of the experimental procedure. After the tribotest, the wear track and wear scar are characterized directly, the “tribo-liquid” between the friction surfaces is extracted by pipette for subsequent characterizations. “a” represents the center position of wear track, “b” represents the original NbB₂ film, and “c” represents the center position of wear scar. (b) Raman spectra of wear track, original NbB₂ film and wear scar. In addition to the peaks from spontaneous oxidation on the NbB₂ film surface, more peaks of H₃BO₃ and Nb₂O₅ with higher intensity appeared on the tribopairs. (c) XPS Nb 3d and B 1s spectra of the NbB₂ film wear track. (d) FT-IR spectrum of the tribo-liquid collected after the tribotest. H₃BO₃ and Nb₂O₅ are the main tribo-products dissolved in the water droplet. (e) HRTEM images of the particles in the tribo-liquid. The amorphous H₃BO₃ matrix contains a large number of well dispersed Nb₂O₅ nanoparticles.

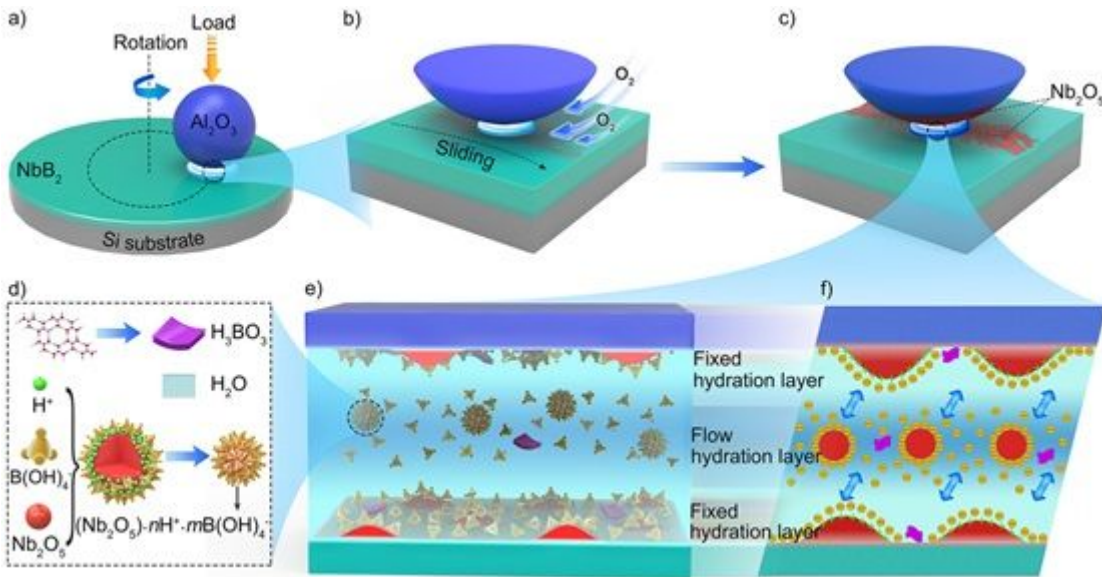


Figure 4

Schematics of the model and mechanisms for superlubricating hydrated NbB₂ film. Illustration of (a) the ball-on-disk loading setup for the tribotest on the hydrated NbB₂ film, (b) the frictional sliding process in the ambient air that supplies the oxygen needed for the tribochemical reactions, and (c) the resultant Nb₂O₅ and (d) other species that promote a series of reactions including oxidation, ionization, adsorption and complexation to form the tribo-products ($[\text{Nb}_2\text{O}_5] \cdot n\text{H}^+ \cdot m\text{B}(\text{OH})_4^-$ and $\text{B}(\text{OH})_4^-$), which lead to the formation of (e) two fixed hydration layers and a flowing hydration layer between the friction surfaces, where (f) the ionic repulsion helps to reduce the contact pressure and the associated friction, thereby facilitating realization of the SL state.

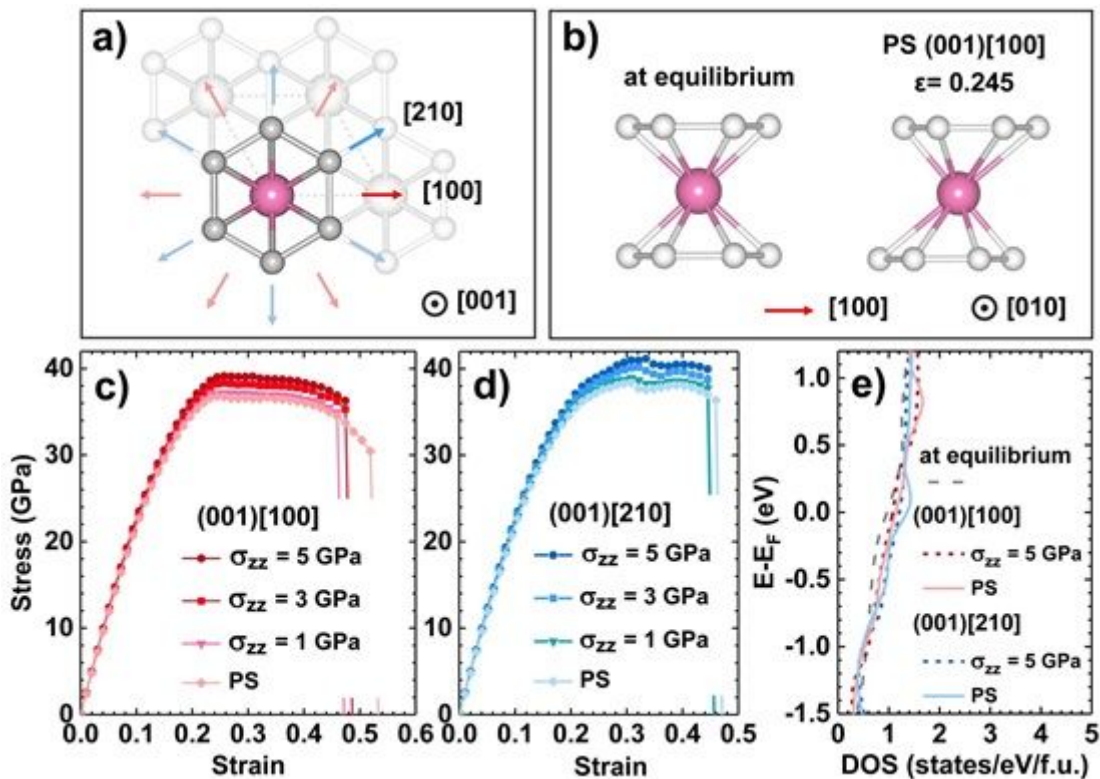


Figure 5

Atomistic mechanism for the superlow wear rate and metallicity of the NbB₂ film. (a) The crystal structure of NbB₂ at equilibrium exhibiting sixfold rotational symmetry in the (001) plane, with the large and small balls represent the Nb and B atoms, respectively. The two major high-symmetry directions, [100] and [210], are indicated by the heavy-shaded arrows, along with the respective five additional equivalent directions for each case shown by the light-shaded arrows in the same colors. (b) The bonding pattern of the NbB₂ structural unit under the pure shear strains along the (001)[100] direction at the peak stress compared with the unstrained equilibrium structure. (c,d) The stress responses to the pure shear (PS) and biaxial (with an additional normal stress s_{zz} that is set at several values) strains in the (001)[100] and (001)[210] shear-slip direction as indicated. (e) Calculated electronic density of states of the NbB₂ crystal that is at the unstrained equilibrium structure, at the peak stress points under the (001)[100] and (001)[210] pure shear strains, or at the peak stress points under the corresponding biaxial strains with the normal stress $s_{zz} = 5$ GPa.

Supplementary Files

This is a list of supplementary files associated with this preprint. Click to download.

- [SLNbB2SupplementaryInformation.docx](#)